HAL open science

A Multifunctional Hybrid Graphene and Microfluidic Platform to Interface Topological Neuron Networks

Victor Dupuit, Océane Terral, Guillaume Bres, Arnaud Claudel, Bruno Fernandez, Anne Briançon-Marjollet, Cécile Delacour

To cite this version:

Victor Dupuit, Océane Terral, Guillaume Bres, Arnaud Claudel, Bruno Fernandez, et al.. A Multifunctional Hybrid Graphene and Microfluidic Platform to Interface Topological Neuron Networks. Advanced Functional Materials, 2022, 32 (49), pp.2207001. 10.1002/adfm.202207001 . hal-04305974

HAL Id: hal-04305974

https://hal.science/hal-04305974

Submitted on 27 Nov 2023

HAL is a multi-disciplinary open access archive for the deposit and dissemination of scientific research documents, whether they are published or not. The documents may come from teaching and research institutions in France or abroad, or from public or private research centers.

L'archive ouverte pluridisciplinaire **HAL**, est destinée au dépôt et à la diffusion de documents scientifiques de niveau recherche, publiés ou non, émanant des établissements d'enseignement et de recherche français ou étrangers, des laboratoires publics ou privés.

A multifunctional hybrid graphene and microfluidic platform to interface topological neuron networks

V. Dupuit,[1] O. Terral,[1] G. Bres,[1] A. Claudel,[1] B. Fernandez,[1] A. Briançon-Marjollet,[2] C. Delacour[1*]

1 Institut Néel, University Grenoble Alpes, CNRS, Grenoble INP, 38000 Grenoble, France
2 Grenoble Alpes, HP2 Laboratory, Institut National de la Santé et de la Recherche Médicale U1300, Grenoble, France

Corresponding author: cecile.delacour@neel.cnrs.fr

Keywords: nanoelectronics, neuron network, graphene, field effect transistor, microelectrode, lab-on-chip, microfluidic

Abstract. The nervous system is as complex as difficult to probe. Innovative tools reducing the network complexity and being able to interrogate neurons are crucial to better understand its function and organization. In this work, solution-gated graphene field effect transistors GFETs are combined with multi-compartment microfluidic platform for multimodal and long-lasting recording of neuron electrical activity. The fluidic microchannels, somatic and synaptic chambers enable to define the neuron network topology, while the graphene devices provide localized, highly sensitive and optically transparent sensing sites. Immunofluorescence staining assesses for the healthy state and outgrowth of neurons within the microfluidic circuit, while calcium imaging demonstrates the maturation and spontaneous activity of the designed network. The efficient cell-sensor alignment obtained by the microfluidic circuit enables to reach the highest reported signal-to-noise ratio for single-units detection with GFETs, revealing additional information that could remain hidden from recordings when using conventional microelectrode arrays (MEAs). Thus, the combination of graphene sensors and microfluidic

circuits leverages the advantages of two state-of-the-art technologies for highly efficient sensing of model neural networks. Being fully transparent and therefore compatible with optogenetic tools and high-resolution microscopy, this novel platform could provide a versatile lab-on-chip for diagnosis and treatment of tomorrow.

1. INTRODUCTION

To assess the function and organization of neural networks, an important requirement is to interrogate the same neurons for a long period of time and within a defined network topology. For that purpose, electronic devices have been used since the beginning of bioelectricity and electrophysiology, because they can both stimulate and record electrical activity of neurons.[1–4] Numerous materials and designs have been developed leading to state-of-the-art high-density microelectrode arrays and which are based on a silicon technology.[5–8] But still several challenges remain to assess brain computational processes. Among them, is the ability to follow spikes propagation (action potentials APs and sub-threshold signals) along individual cells and large networks. This requires highly sensitive and microscale sensing devices, accurate and long-lasting cell-device coupling and to identify the origin of the sensed signals, or in other term the type and position of the sensed-cells.[9]

Although they have been widely developed, conventional metallic microelectrodes face physical limitations to tackle these challenging goals, especially regarding their sensitivity[9] and time stability.[10] The signal-to-noise ratio increasing with the sensors area, the microelectrodes have to remain large (30 µm diameter typically). But because of their large size in comparison with a soma or a neurite (about 15 and 2 µm respectively) and because the detection is extracellular, the microelectrodes sum many signals. As a result, it is difficult to identify the origins of the recorded signal and to differentiate physiologically-relevant signals from electrical noise. This limits their detection efficiency and prevents from measuring other and often weaker signals than action potentials. Alternatively, field effect transistors FETs are

promising candidates for highly sensitive extracellular detection, providing the possibility to increase the sensitivity while reducing the sensor size. The FETs sensitivity is proportional to the width over length (W/L) ratio of the transistor channel, while the MEA's sensitivity is rather proportional to the electrode surface area. Thus, the FET size can be reduced at sub-cellular scale (up to 10 nm for silicon nanowires) while reaching higher sensitivity values than with MEA.

First demonstrations were provided with the implementation of silicon-nanowire field effect transistor SiNW-FET arrays for monitoring single spike propagation within individual neurons[11–13]. Also, other materials have emerged such as organic[14] and 2D materials[15] which provide novel advantages compared with the classic silicon technology such as flexibility, optical transparency and softness to improve mechanical compliance of the sample with neurons and therefore its biocompatibility. In particular, graphene, a semi-metallic monolayer of carbon atoms, provides an ideal platform for recording and culturing neurons. Because of its 2D nature, its high carriers' mobility and its high chemical stability, a high sensitivity regime can be achieved within graphene FETs which exceeds the threshold performance of silicon technology while keeping high frequency operation and high-density integration possibilities. Today, arrays of graphene field effect transistors can be implemented with reliable sensing performances,[16] and could be compatible with high-density implementation at manufacturing level.

Since the first demonstrations for biosensing, graphene has been successfully used for neural interfaces, providing the required sensitivity for the detection of neuronal signals, such as infralow frequency oscillations and local field potentials,[17–19] single spikes from individual neurons,[16,20] and ultimately synaptic and ion channel currents.[21–23] An additional advantage when interfacing neurons is its optical transparency. Absorbing merely 2.3% of incident light,[24] graphene is compatible with high-resolution transmission imaging and optical-modulation of neuron activity. The given ability to observe and manipulate cells at the sensing sites with

optical tools is of great scientific interest, such to identify the spiking neurons which are recorded, as well as to tailor safe stimulation and correlate several features of cell metabolism (e.g. voltage, calcium, temperature variations).[25] Furthermore, due to its strength, its flexibility, and its biocompatibility, graphene promotes cell attachment[26,27] to achieve long lasting and strong electrical coupling with neurons, thus high detection efficiency are expected for a long-term experiment.[28] The unique combination of all these bio-suitable features makes graphene an excellent material for neural interfaces and biosensing in general.

Here we demonstrate the ability to combine graphene electronics with microfluidic circuits which will lastly reduce the complexity of neuron networks in-vitro and provide the required accurate and long-lasting electrical coupling with the cells to be sensed. This combination of state-of-the-art sensors and microfluidic circuits leverages the advantages of both technologies for monitoring activity of neurons within designable architectures and during the maturation time of the network. After ground breaking experiments for studying axonal regeneration, microfluidic circuits have become one of the most efficient approach to build long lasting neuronal architecture in-vitro.[29–34] This approach supports neuron attachment and neurite spreading in large somatic chambers, while micrometer-wide fluidic channels could select and guide the axon outgrowth above the sensing sites with geometrical constraints only. Thus, neuronal network with a user-defined topology can be cultured during weeks within the microfluidic circuits, and be electrically connected with array of planar devices integrated on the underlying substrate to study neuronal network functions.[35–37] In that emerging field, graphene devices could provide a higher sensitivity and spike detection efficiency. Also, being fully transparent and therefore compatible with optogenetic tools and high-resolution microscopy, the reported graphene sensing platform opens the door for avenue of innovative investigations *in-vitro* combining optoelectronic addressing (recording and stimulation) at the same cell location.

Beside the fabrication of the state-of-the-art graphene device arrays and the ability to culture healthy neurons within microfluidic environments, one difficulty is to assemble the GFET array and the microfluidic circuit and fill it with liquids without compromising the fragile graphene sensors. In particular, a process that we commonly use (oxygen plasma) to render hydrophilic the surface of both the devices and microfluidic substrates, cannot be used as it would etch the graphene sensing part.

In this work, we show how to fabricate and align graphene field effect transistors with microfluidic circuits for culturing and sensing primary neurons. The final architecture and electrical maturation of the obtained neuron network have been assessed with immunofluorescent staining and calcium imaging, while the spike detection performance of GFETs have been compared with graphene and standard TiN microelectrodes.

2. Combining graphene sensors and microfluidic circuits for interfacing topological neuron networks

a. Manufacturing transparent GFETs arrays

The arrays of graphene field effect transistors are fabricated on α-Al_2O_3(0001) c-plane sapphire substrates (figure 1a) from graphene monolayer grown by thermal chemical vapor deposition. Briefly, graphene was grown on 25 µm thick Cu foil previously cleaned in acetone and annealed at 1000°C in diluted H2 environment for 2 hours (dilution in Ar at 10%). Then, a small flow rate of CH4 was injected as a carbon source (1000 sccm, 25 mbar pressure). The cm^2-large pieces of graphene are then transferred on the sapphire substrate (44 x 44 mm^2) by polymer (PMMA) assisted wet transfer technique. The Cu/graphene samples were covered by a PMMA supporting layer, and the Cu foil was then etched in diluted ammonium persulfate $(NH_4)_2S_2O_8$ solution (0.1 g/ml at room temperature). The remaining graphene-PMMA bilayer was rinsed in successive deionized water baths to remove etchant residuals. The bilayers are finally pulled

from the solution with the sapphire substrate.[38] Directly after fishing, the sample is dried at room temperature for several hours, followed by heating steps at 120°C to dehydrate the sample. Then, PMMA layer is removed in an overnight acetone bath. Residues were further decomposed by annealing at 350°C for 2h in ultra-high vacuum.

The quality of the transferred graphene monolayer was then assessed by Raman micro-spectroscopy (commercial Witec Alpha 500 setup and laser excitation wavelength λ_{exc} = 532 nm). The integrated intensity ratio I_G/I_{2D} ~ 0.3 between the G and 2D bands (centered at 2674 cm^{-1} and 1585 cm^{-1} respectively), and the narrow width of the 2D band ω_{2D}= 25 cm^{-1} are clear signatures of the monolayer nature of the graphene sheet (figure 1b).[39,40] The low intensities of the defect-related D and D' bands (1350 cm^{-1} and ~1620 cm^{-1} resp.) further reveal the overall high quality of the transferred monolayer graphene. This was confirmed with the atomic force micrography (figure 1c). Few localized resist residuals remain on the graphene top surface, in addition with the typical wrinkles resulting from the wet transfer technique.

The graphene devices were then fabricated according to the process illustrated figure 1d. A hard mask (10nm-thick Au) was used to define the transistor channels and to prevent graphene to be exposed to the optical resist. Outside the channel, graphene was etched in oxygen RIE plasma, and the hard mask was then etched in diluted potassium iodide solution (1min). Then metallic leads were obtained by UV lithography of S1805-photoresist, followed by the evaporation of 0.5 nm Ti, 30 nm Pd and 20 nm Au, finally lifted-off in *N*-Methyl-2-pyrrolidone (NMP) at 80°C. The last step aims to passivate the metallic leads with a thick and biocompatible layer of SU8 resist, and to expose the graphene transistor channel to liquid. Lastly a layer of 2 nm hafnium oxide $Hf0_2$ was deposited by atomic layer deposition (at 110°C) over the whole sample surface. This ultra-thin high-κ dielectric protects the graphene channels without altering its electrical performance. Thus, advanced cleaning process can be performed after the cell experiments to recycle the chips. The optical micrograph shown within figure 1e illustrates the high-quality surface of the graphene FET channel as obtained at the end of the microfabrication process, and

which is as exposed to cells and liquid for sensing operation. Between each day of manufacturing and until use after completion, the GFET chips were stored under primary vacuum.

The two-wire resistance was measured over 50 tested devices in dry conditions. The obtained values $R_{2W} = 2 \pm 0.1 k\Omega$ demonstrate the reproducibility of the fabrication process. Also, the resistance per contact measured by the transmission line method (TLM) Rc = 0.25 ± 0.03 kΩ is lower than previously reported values[16] and further confirms the high quality of the monolayer graphene and the ohmic nature of the contacts. The square resistance of the graphene sheet was then extracted from the two-point resistance and contact resistance. Given the channel length L and width W of 30 µm and 20 µm respectively, the measured square resistance is about $R_{\square} = 1 \pm 0.1$ kΩ/□, being slightly higher than values obtained with pulsed-CVD grown graphene monolayers.[16] Indeed, the pulsed growth method is expected to provide larger grains size and fewer multi-patches, which could explain the discrepancy observed with the continuous CVD-growth used here (continuous CH4-flow); all other parameters revealing the high quality of the micro-fabrication process.

The field-effect detection was then assessed by measuring the graphene channel conductance while varying the liquid top-gate. The liquid-gate voltage V_{LG} was applied to an Ag/AgCl electrode (few mm^3) immersed into saline solution and the graphene transistor channels were biased with a constant drain voltage V_{DS} = 60mV while monitoring the drain current I_D with a variable gain current amplifier (Femto Messtechnik GmbH, DLPCA-200). To reduce electrical noise, samples were placed in a Faraday cage, and all the electrical lines were band-pass filtered (200 Hz – 4 kHz). The power spectral density of the GFETs shows the typical 1/f shape and a noise level at 1kHz of about 10^{-22} A^2/Hz, that are as expected for GFET (figure S8). The conductance G of the graphene GFET is efficiently modulated by varying the liquid-gate voltage (figure 1f). Increasing the gate potential tunes the GFETs from the hole to the electron operation regime. First the conductance decreases due to the depletion of the hole carriers

reaching a minimum value at the Dirac point (V_D ranging between 0.7V - 0.8V). Then, the channel conductance increases resulting from the accumulation of electron carriers within the transistor channel. The maximum of conductance is reached in the hole regime, suggesting a positive doping of the monolayer due to negatively-charged residuals or surface-charge traps at the substrate and liquid interfaces. The double peak measured at the Dirac point is a common feature that we observe when using sapphire substrate,[16] and that we associate to charges trapped and electrostatic interactions at the lower graphene-sapphire interface.

The device sensitivity S is then extracted from the (I_D-V_{LG}) curves, as defined by the transconductance $g_m = \partial I_D / \partial V_{LG}$ normalized by the drain voltage V_D (right axis figure 1f). The maximal sensitivity values ±2,3 mS/V are as expected for GFETs on sapphire,[16] being higher than value reported for silicon.[20] The optimal operation regime for bio-sensing, being here in the hole conduction regime at V_{LG} = 0.75V. From the GFETs transconductance, we estimate the charge carrier's mobility μ according to the following formula:

$$S = g_m \times \frac{1}{V_D} = \mu \cdot C_G \cdot \frac{W}{L} \qquad (1)$$

with C_G the graphene capacitance at the top graphene interface (with the solution) measured in double back and front gates configuration on a reference silicon-on-insulator SOI substrate (C_G = 0.78 μF/cm^2). Considering the exposed graphene area being 10 μm long and 20 μm width (figure 1e), the estimated mobility is μ_{eff} = 1474 cm^2·V^{-1}·s^{-1} in the hole operation regime, which agrees with typical values obtained on sapphire.[41]

b. Microfluidic neural networks and their coupling with GFETs arrays

The microfluidic platform was designed to guide neurons and in particular their axons above the GFET array as depicted within figure 2a (detailed in the experimental section). The fabrication protocol was adapted from several seminal works as detailed below. First, the fluidic circuit was composed of two large somatic chambers (40 μm high) joined by an array of 3 μm

high and 7 µm wide microchannels. This architecture allows to seed two distinct neuron populations with a controlled connectivity, defined by the density of interconnecting microchannels. In our design, we integrated supplementary elements to force the directionality of neuronal spikes propagation. Mainly, this requires to control the axons position and outgrowth. To that aim, we implemented a first array of long channels (400 µm) that is expected to select axons only,[29] while a second one with shorter microchannels (100 µm) could contain all neurites indiscriminately, including dendrites. A central synaptic chamber[35] separated the two fluidic channels arrays, where axons from the expected efferent population could connect with the dendrites of the afferent population (figure 2a). Additional neurite traps[31] prevent neurites from the efferent population to explore further than the synaptic chamber (short dead-end microchannels as shown figure 3a). Lastly, neurite funnels on the efferent side increase the probability of guiding axons inside the microchannels (figure 2b).

The micrographs of immunofluorescent stained neurons have been performed after the cultures in the microfluidic architectures. As detailed in the "Experimental section", primary neurons were extracted from hippocampi or cortex of mouse embryos (E16) and seeded within the large somatic chambers; the exposed substrate being previously coated with poly-L-lysin to promote neurons attachment and outgrowth. Then neurons were immunostained with anti-alpha tubulin and DAPI (1:1000, Millipore) to label the cytoskeleton and the nucleus respectively. In the somatic chambers, neurons have efficiently attached and outspread such as the neurites cover the entire chamber surface. Interestingly, the micrograph demonstrates that all the fluidic microchannels are explored by neurites after three weeks in culture, even in simple microfluidic architectures (figure 2c).

In addition, we assessed the ability to combine the microfluidic environment with optical imaging of neurons activity. For that purpose, we loaded the cells with a broadly-used calcium-sensitive fluorescent indicator Fluo4. Figure 3 shows the live imaging of calcium activity within the loaded neurons. Through the PDMS chip, we observed the neurites spreading within the

designed microfluidic circuit which is as described within figure 2. The neurites explored both the long axonal and the short dendritic microchannels, and efficiently meet within the synaptic chamber (larger view shown within figure S2). Also, the time course of the fluorescent intensity has been acquired over several time-series and showed transient calcium currents associated to spontaneous firing activity of neurons. These calcium currents can be detected at multiple scales within both the neurites and the somatic chambers (right plots figure 3a and 3b respectively). While clear neuronal signals emerge within the somatic and synaptic chambers, weaker but still detectable signals are measured within the microchannels guiding the neurites above the GFETs (green time-trace within figure 3a). The signal-to-noise ratio is the highest when illuminating in backside through the transparent substrate (figure 3) in comparison with the front-side illumination (figure S2). But still the background of fluorescence from the PDMS microfluidic circuit hides most of the transient Ca^{2+} currents and specially along the walls of the micro-channels where neurites preferentially develop and where the signal-to-noise ratio is the lowest S/N=2 versus 10 within the somatic chamber (red and orange versus green time-traces, figure 3a). Advanced fluorescent indicators such as genetically encoded indictors (GECIs or GEVIs) could improve that feature, but this could remain a possible limitation of optical imaging within the PDMS-microfluidic circuit that would need future improvements. Overall, these results confirm the ability to define the neuron network topology and specially to guide the neurites along axonal highways while keeping healthy neurons during weeks within the microfluidic circuit, as well as the possibility to image spontaneous activity with fluorescent indicators. Although calcic imaging (figure 3 and S2) shows signals propagating from the efferent population to the afferent population, dedicated experiments are required to demonstrate this firmly. Here, we only assume this directionality based on the design rules that have been detailed previously.

After succeeding the culture assays, the microfluidic circuits were aligned with the GFET arrays and stacked on the sapphire substrate as previously shown within figure 1a. This step was

performed manually with an inverted microscope, and could lead to 80% of perfect match between the GFETs and fluidic channels (figure 2d-f). This alignment could be further improved with dedicated marks and motorized in-plane and out-of-plane (x, y, z) movements of the sapphire GFET substrate relative to the microfluidic PDMS chip. Then, neurons were seeded within the somatic chambers and attached on the exposed sapphire surface previously coated with poly-L-lysin.

The high optical transparency of the GFETs and the neurofluidic circuits (figure 1a) enables to observe neurons with an inverted phase-contrast microscope along the culture time. Figure 2d illustrates the typical healthy shape of neurons after 10 days in culture; the neurons on glass and sapphire chip outgrew similarly. In particular, we did not observe any cluster of soma or neurite bundle (zoomed-view figure S3) which are typical signatures of hostile micro-environment or cellular stress. At the opposite, the attached somas remain homogeneously dispersed within the somatic chamber. Thus, we can expect similar neurite spreading within the microchannels as the one observed on the glass coverslips. Also, neurites could be observed hitting the tapers at the entrance of microchannels (figure 2) and progressing within the axonal microchannels towards the synaptic chamber. The axons spread straight along the microchannel walls, as observed at the channel exit (figure 2f). As a second important result after the primary culture assays, these optical micrographs demonstrate that microchannels guide the neurites above the transistor graphene channels, providing accurate and long-lasting alignment of axons and dendrites over the sensing sites. Also, note that single neurite exits the fluidic microchannels, that could enable studying spike propagation within individual cell.

3. Operando measurements of single-units with graphene field effect transistors

Once the ability of culturing and guiding neurons within the microfluidic circuit were demonstrated, as well as the accurate and long-lasting neurite-GFET alignments were obtained, we assessed the electrical performances of the GFETs for recording neuronal spikes. For this

purpose, a dedicated connector has been developed that contacts a quarter of the devices in the sample (16 contacts over 64), and that enables to switch manually from one to another GFET (figure S1A). The sample being symmetric, all the GFETs can be measured by rotating the chip by a quarter turn. In that way, still only two transistors at a time can be measured, but this facilitates and accelerates the devices connection in comparison with the multiprobe station used for the electrical characterizations (Part 2).

For each measurement, the drain-current time-trace series have been acquired at 50 kHz sampling rate with two amplification stages (detailed in the "Experimental section"). The graphene FET was biased at constant drain voltage (60 - 75 mV) while the current was monitored with a variable gain amplifier which includes a current to voltage converter (figure S1B). The low frequency component (mainly the DC-current) can be removed and the signal further amplified by a factor 100 (figure S1C).

Figure shows the equivalent gate voltage time course of a GFET, while recording a volley of spikes which we attributed to the spontaneous activity of the neurite populating the microchannel (raw data of the drain-current $I_D(t)$ are shown within figure S5a). Inside a single volley, the inter spike interval could be very stable (16 ms ± 300 µs on 10 spikes, figure 4d) which is a clear signature of single neuron activity. To our knowledge, this is the first reported proof of concept of individual neurite activity measured in a fluidic microchannel with a graphene field-effect transistor. The amplitude of the detected spike is also much higher than the previously reported values (×10), measured under same culture conditions but without microfluidic circuit and with the same type of devices.[16,20]

The extracellular voltage was calculated according to the following formula,

$$\Delta V_{extra}(t) = \left(\frac{\partial I_D}{\partial V_G}\right)^{-1} \cdot \Delta I_D(t) = \frac{\Delta I_D(t)}{V_D \times g_m} \qquad (2)$$

as a function of the GFET response $I_D(t)$, the normalized transductance g_m (-2.3 mS/V for V_{LG} = 0.75 V) and the drain voltage (V_D = 75mV). During spiking events, the variation of the

extracellular voltage ranges between ΔV_{extra} = [- 56 μV; -117 μV] with an amplitude and polarity which are as expected for primary neurons. Note that the detection of spikes was performed at early stage, between seven and ten days of culture, sometimes earlier (DIV4) which is occurring only within the microchannels. Otherwise those signals remain extremely rare or even absent from the recordings even when using conventional microelectrode array. Spontaneous activity appears rather after 11 days in culture outside the microchannels.

Important to notice is also the shape of the GFETs response. As observed in figure 4d, the time course of GFET signals are very similar to the form of intracellular spike (figure S4) with an inverted polarity. The signal is commonly biphasic, starting with a sharp transient followed by a weaker negative peak before returning to the resting value. There is no additional peak as usually observed with MEAs (figure 5) that are faradic currents artefact. Figure 6 compares the GFET response, with the expected extracellular potential V_E (in the hole operation regime) and the intracellular potential V_{Intra} measured in patch clamp (whole cell mode). As illustrated, the GFET recordings could provide a close copy of the intracellular signal shape while keeping an extracellular measurement.

Several signal shapes (polarity and amplitude) measured with the GFETs reveal differences in the sensed-neuronal-spikes. To compare them and simultaneously check the devices response, we applied a short positive and gaussian shaped voltage impulse V_P (1mV, 1ms) within the liquid gate, namely an artificial spike that closely mimics a biological signal. Thus, in a same time-window, we could assess the GFET response to the artificial impulse and the neuron spikes. The time-traces of the recorded signals are shown in supplementary figure S5, and the main features of the detected spikes are reported within the following table 1.

Signal	Amplitude (nA)	Duration (ms)	Extra-cell. spike (µV)	Noise (VPP)	SNR
Spike_1A	-49.4	1.67	358	3.6	13.7
Spike_1B	-32.3	0.73	234	3.6	8.9
Impulse_1	-11.9	1.19	86	3.6	3.3
Spike_2A	76.3	2.6	-553	21.4	3.6
Spike_2B	45.7	0.73	-331	21.4	2.1
Impulse_2	-15.3	0.8	111	21.4	0.7
Spike_3A	-137.3	1.4	796	18.3	7.5
Spike_3B	-122.1	1.27	709	18.3	6.7
Impulse_3	-12.2	1.2	70	18.3	0.7
Spike_4	+31.7	4.5	-184	6.9	4.6

Table 1. Main features of the evoked neuronal spikes recorded with the GFETs. The time-trace series from 1 to 4 are reported within figure S5b. Spike and impulse labels are used to differentiate the GFETs response induced by the top gating neurons from the response induced by the short artificial pulse (1mV and 1ms) applied with the gate electrode (30 µm-width Au microelectrode). The latter being used to assess the reliability of the device responses.

First, note that the GFET responses recorded when applying the phantom spikes remain the same in term of amplitude and polarity for all recorded devices; being 1 ms duration and -13 nA amplitude with a negative polarity which is as expected in hole operation regime. The ratio between the applied and the effective amplitudes of the gate voltage is significantly reduced $V_p/V_p^{eff} = 10.5$, with V_p^{eff} being calculated from the current modulation ΔI_D and the device transconductance g_m (-2.3 mS/V, in the hole operation regime). The gating electrode being far from the devices located inside the microchannel, the observed drop of the gate voltage is associated to the resistance of the microchannels.

At the opposite, the drain current variations ΔI_D induced by the top neurites are much higher, between ten and three times higher for the same device, and lead to extracellular voltage ranging from 234 µV and 796 µV, estimated from ΔI_D and g_m values according to equation (2). Both positive and negative signals are measured, that could stem from inhibitory and excitatory post-synaptic signals (EPSP/IPSP) within a dendrite. Glutamatergic and GABAergic neurons are indeed expected in similar proportion at this culture stage in our culture (figure S6), thus both can connect the target neurite which is currently sensed. Overall, for all the recorded signals,

we first observed a rapid increase of current (absolute value) followed by a longer decay component before returning to the baseline value. The signals shape is still monophasic and closely follows the expected variation of intracellular signals (figure 4d, 5 and S5). Few time-traces exhibit multi-peaks (e.g. Spike 1A, Spike 2B, Spike 4 within figure S5b) which could originate from spike train within individual neurites or collective spiking events within few neurites if any within a same microchannel, as few neurites are observed within the microchannels (figures 2c and 3a).

Finally, the state of each working transistor could be assessed by acquiring *in situ* the transfer (I_D-V_{LG}) curve versus the gold gate electrode in the nearest chamber (figure 2d). Those gates were used in order to not insert another reference which could contaminate our samples and prevent data acquisition in the following days. In this configuration, the transconductance of our devices appears different (figure S7). The drain current modulation is reduced by a factor 1/10 in comparison with preliminary characterizations without the microfluidic circuit and the cells (figure 1f). Also, the charge neutrality point V_D is shifted towards higher values of the gate voltage. Both could be explained by the voltage drop within the resistive microchannel. As discussed previously, the effective gate voltage V_{LG}^{eff} sensed by the GFET within the microchannel is reduced by about ten in comparison with the bias value V_{LG}. This is due to the high resistance of the microfluidic channel. The shift of the Dirac potential V_D could be associated to the nature of the gating electrode, however noble metal such as Au rather shifts the Dirac point toward lower gate voltage value. [20] Also, a shift of the Dirac point could result from the adhesion of the negatively charged cell membrane on the FET channel, and from the ionic strength of the culture medium.[20] Further studies are required to investigate their effects and set the proper conditions (design, material, location, size of the reference electrode) to optimize the gating condition within the microfluidic platform. Dedicated design for the gate electrodes could prevent such artefacts, for instance by adding local gate electrodes within the

microchannels or a bottom back-gate. Although it does not alter the spike detection, it could be useful for exploiting further the spikes form acquired with the GFETs.

4. Benchmarking G-FET and G-MEA sensors for multiunits recordings

Once the detection of unitary spike was validated with the GFETs, we have further assessed their performance in comparison with GMEA and commercially available metallic MEA (TiN, 30 µm wide). Figure 5 illustrates the voltage time-traces acquired with the graphene (a) and the TiN (b) microelectrodes. Sharp pulses are observed within both voltage-time traces that are clear signatures of neuronal spikes, which already demonstrates the ability to use the same graphene device as a transistor and as an electrode for the detection of neural activity. In opposition to the FET-operation regime, the recorded signals are triphasic (zoomed views figure 5a) with a higher negative peak, which is as expected for MEA recordings. The amplitude of MEA signals should be proportional to the extracellular potential as the following expression:

$$V_{MEA} = \frac{C_{JE}}{C_E + C_L} \times V_{extra} = \frac{A_{JE}}{A_E} \times V_{extra} \qquad (2)$$

where C_{JE} and C_E are the capacitances of the cell-covered and entire areas of the electrode, of sizes A_{JE} and A_E respectively. With a negligible value of the ohmic contacts capacitance C_L, the amplitude of the recorded signal depends linearly on the ratio of the covered electrode area and the entire electrode area.[42] The size of the exposed surface of the TiN (300 µm²) and the graphene (70 µm²) electrodes should favor the TiN-MEA in term of signal and noise level (see optical micrographs of the devices within figure 5), also the impedance being higher for the graphene devices over the entire spectral range (figure S9).[43] At the contrary, the peak-to-peak amplitude are higher for the GMEA (about 95 µV) than for the metallic MEA (75 µV). Moreover, using the graphene microelectrodes led to a better noise level. Thus, the GMEA provides the highest signal-to-noise ratio S/N~12, widely exceeding the performance of the TiN-MEA (S/N = 4) under the same recording and culturing conditions.

The spikes form measured with the graphene and the TiN MEA exhibits some discrepancies (amplitude, rise and decay time). These differences could result from the capacitive and faradic components of each microelectrode impedance and from the cell-device interface (figure 6). This last component is dominated by the adhesion of the cells on the electrode. As reported in several works, including ours, graphene promotes adhesion of neurons that could indeed favors a close contact (in other term an ultra-thin junction), leading to higher value of the sealing resistance R_{seal}. The position of the cell in respect with the sensing area also could impact the signal form. In the microchannels however, the neurites are perfectly aligned with the device. Thus, it unlikely explains the observed discrepancies in the shape of the measured signals. Lastly, the nature and size of the reference grounded electrode are different which could have a significant impact also on the shape and amplitude of the recorded signals

Interestingly to note, is the presence of secondary spikes of lower amplitude that could follow the first spikes of higher amplitude. There are underlined with the blue and red bars respectively within each voltage-time traces and raster plots figure 5a and 5b. Although the amplitude of these spikes remains lower, they are clearly resolved with the GMEA. However, it remains difficult to extract those from the background noise within the TiN-MEA time-trace (raster plot, figure 5b). This result demonstrates further the high detection efficiency that could be reached with the graphene devices.

Regarding the GFET signals on a same time interval (ie between two primary spikes of highest amplitude), a multitude of secondary spikes are also measured (figure 4a) that strongly resemble to the secondary spikes measured in GMEA-mode. If we consider that the interfaced neurites have a similar excitability, this result suggests a higher detection efficiency with the graphene FETs; the number of secondary spikes which are measured during one interval being 10 versus 2 for GFET and GMEA respectively. This effect is also observed when using intracellular patch clamp measurements (figure S4b, red curve) and usually associated to the depletion of ion reserves. Here we show, that graphene devices coupled with fluidic microchannels enable to

detect those weaker spikes than are not observed as clearly when using TiN microelectrodes. Thus, both GFETs and GMEAs provide transparent and highly sensitive devices, and could be used in concomitant for multimodal detection of neuronal spikes. Todays, the GMEAs benefit from advanced acquisition setup (commercially available) including multisite recording and real-time signal filtering, that have been broadly developed since the 1980's. At the opposite GFETs could suffer from the need of a dedicated electronic (not yet commercialized) which currently limits their application to few academic labs. Although two devices at a time could be measured in this study, current developments of dedicated electronics for multiple addressing provide promising perspective.[44,45] In particular, a unique advantage of GFETs is the ability to use multiplexed frequency addressing that enable high-density integration and fast readout possibilities, which are key requirements for high spatiotemporal mapping of electrical activity of cells.

5. CONCLUSION

We have shown the ability to combine highly versatile and ultra-performant graphene devices with topology-controlled neural network in-vitro. First, we demonstrated that arrays of graphene field effect transistors can be efficiently aligned with fluidic microchannels, while keeping both the high electrical performance of GFET (i) and the high hydrophilicity of the microfluidic circuits to convey liquids and cells above the GFETs within few micrometer wide channels (ii). The culture and outgrowth of primary hippocampal and cortical neurons were successfully obtained within the microfluidic circuit; neurons have efficiently attached within the large somatic chambers, while the microchannels enabled the further growth and selection of neurites over the sensing sites. Thus, beyond controlling the neural network topology, combining GFETs and microfluidic circuits offers a long-lasting coupling of the neurites and the electrical devices that optimizes neural spikes detection. The electrical recordings of neural bursts and single units demonstrated the high detection efficiency obtained by combining the

fluidic microchannels and the transparent graphene devices, that outperform conventional TiN microelectrodes. In particular, this platform enabled us to detect clear signatures of spontaneous neuronal activity even at early stage of the culture, providing additional information within the spike shape and amplitude than with TiN-MEA recordings. Moreover, we show that graphene devices can be read in both MEA and FET operations, illustrating further the versatility of the reported sensing platform. The GMEA have been widely studied since the past years compared to GFET. They benefit from the acquisition electronics and post-signal analysis developed for the MEAs, while keeping all advantages of the graphene material. The ability to use the same device both as transistors and as a microelectrode is a practical advantage to analyze the devices responses and to prevent possible artefact as both measurements could be performed on same cells. In addition to a higher signal-to-noise ratio and detection efficiency, graphene offers many advantages such as its optical transparency allowing optoelectrical imaging in real-time and at the same cell's location. For all these reasons, this original combination offers a promising tool for interfacing topological neuron networks or multifunctional sensing of living matter in general, being useful for both fundamental and applied sciences.

FIGURES AND CAPTIONS

Figure 1. Graphene-field effect transistors manufacturing. (a) Optical micrograph of the final hybrid device combining the GFET array and the microfluidic circuit, all integrated on transparent sapphire substrate. (b) Typical Raman spectra of the used CVD-grown graphene monolayer with the typical D', G, D, and 2D bands associated to the graphene crystalline lattice. Spectra has been averaged over 5 measurements acquired at five cardinal points of graphene monolayer transferred on silicon and used as a reference substrate. (c) Atomic force microscopy of graphene monolayer obtained after transfer and annealing in ultra-high-vacuum. The micrograph shows a continuous layer with typical wrinkles and few polymer residues from the PMMA carrier layer. Scale bar 5µm (d) Schematic of the GFETs fabrication steps as detailed in the main text and in the "Experimental section". (e) Optical micrograph representative of the final GFETs, showing the 10 × 20 µm² graphene channel and the two ohmic contacts which are passivated for liquid operation. (f) Conductance G and normalized transconductance g_m of the graphene FET channel as a function of the liquid gate voltage V_{LG} (left and right axis respectively). An Ag/AgCl electrode has been used as a reference electrode.

Figure 2. Design and neuronal culture in the GFET microfluidic assembly. (a) Layout of the device showing the fluidic microchannels over the GFET chip. Full red is the Ti/Pd/Au ohmics surrounded in hatched red by the SU8 passivation layer; purple and dark cyan label the graphene and fluidics respectively. The narrow neurite microchannels are 4 µm high while the large (mm^2) somatic chambers are 40 µm high (left and right). The design intends to be directional with the right chamber (1) sending axons toward the centered synaptic chamber, while dendrites from the left chamber (2) can spread towards the synaptic chamber. (b) Zoomed view of tapered fluidic funnel used to further guide axons above the GFET. (c) Fluorescent micrograph of immuno-stained neurons cultured during 3 weeks in microfluidic circuit. Nuclei are labelled in blue with DAPI, and the cytoskeleton with anti-alpha tubulin (green, FITC) underlying the intricated mesh of neurites. (d) Optical micrograph of living neurons (10 days in culture) cultured within the microfluidic circuit shown in (a) which has been aligned with the GFET array (ohmic contacts appear in black, while graphene FET channels are transparent). The 100 µm wide Au-electrode (labelled REF) is used as a liquid-gate electrode, allowing to set the operation regime of the FETs at the highest sensitivity point. Zoomed view of the entrance (e) and the exit (f) of axonal channels, showing the neurites hitting the funnels at the narrow channels entrance and being channeled further in towards the synaptic chamber and over the GFETs. Few neurites are underlined with the red arrows as examples.

Figure 3. Intracellular Ca^{2+} imaging within the topological network. Neurons have been loaded with Fluo4-AM and recorded in HBSS-HEPES at room temperature. Images and time traces show the spontaneous activity of the neurons within the microfluidic circuit at DIV14. The two FITC-images were acquired in the synaptic (a) and the somatic (b) chambers respectively (40× magnification, backside acquisition through the substrate). On the right of each image, the time course of the fluorescence intensity ratio $\Delta F/F_0$ is given for several regions of interest ROI to show the variations of fluorescent intensity related to Ca^{2+} transient currents, and propagation from the expected efferent to afferent fluidic microchannels (a). Each region of interest is indicated with a circle or an arrow for the soma and the neurites respectively. The color scale is the same for the corresponding time traces (right data plots). The complete time series are provided in Supplementary Information (figure S2 and movies).

Figure 4. Single-units recording with GFETs. (a) Typical time trace recorded with the GFET assemble with the microfluidic chip in which cortical neurons have been cultured. Right micrograph shows the recorded GFET and the accurate alignment with the fluidic microchannel. Acquisition has been performed 10 days after neurons seeding, with a sampling frequency of at 25kHz. The recording is performed in the culture medium, 5 mins after taking out the sample from the incubator. The voltage-time trace exhibits a burst of regularly separated physiological spikes. Highlighted areas show the next plotted regions of interest within (b) and (c) that zoom in the details of the spikes shape. For each time series (a and b), the raster plot has been reported (headband of the time-trace). Each bar corresponds to a spike; the red color indicates the spikes of highest amplitude. The GFET was gated at V_{LG}=750 mV with the quasi-reference Au-electrode (as described figure 2) and polarized at V_D=75mV. The signal was amplified with the two amplification stages as described in the main text.

Figure 5. Single-unit recordings in MEA-operation regime, with the graphene (a) and the TiN (b) microelectrodes. The optical micrographs show each device used and their perfect coupling with the microfluidic axonal channels. Black areas correspond to the metallic leads. The graphene channel remains transparent between the two ohmic contacts. The voltage-time traces have been recorded after 10 days in culture. Each device enables to detect the spontaneous activity of neurons, with typical ms-short pulses. The highlighted areas show the next plotted regions of interest for each graphene and TiN-MEA. All measurements were performed at 25kHz. The Au and Ag/AgCl electrodes have been used as reference electrodes for the graphene and the TiN microelectrode respectively. Also, for each time series, the raster plot has been reported (headband of the time traces). Each bar corresponds to a spike; the red color indicates spikes of highest amplitude. Blue indicates secondary spikes of lower amplitude which occurs between two primary (red) spikes.

Figure 6. Schematics of the neuron-gated GFET and GMEA, showing the experimental measurements of neuronal spikes acquired with the patch clamp (whole cell mode for intra-spike), the GFET and the GMEA respectively; as well as the expected extracellular spike form at the cell-device interface within the cleft. The value and form of the V_{extra} should vary as function of the seal and bath resistance mainly. These values are higher within the microchannels, that leads to higher value of V_{extra} and which thus enhances the detection efficiency within the microchannels. Regarding the spike form acquired with GFET, it closely mimics the shape of intracellular spike, without additional current peaks associated to faradic artefacts as observed with the GMEA. While GMEA provides the highest signal-to-noise ratio, GFET reaches also higher detection efficiency. As a same device could be used either as a transistor and as electrode, the two FE- and ME-detection modes could complete each other.

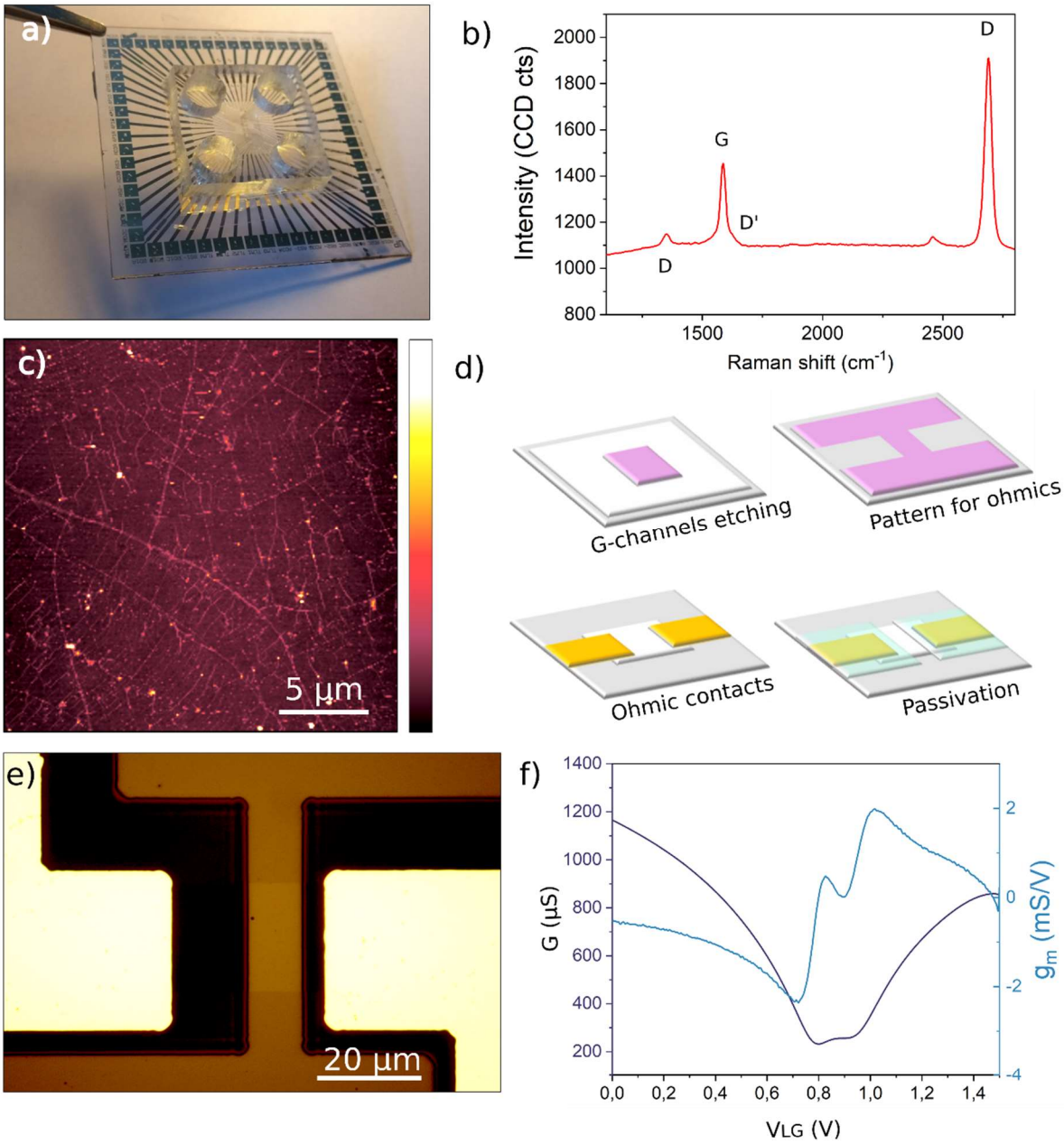
a)
b)
Intensity (CCD cts)
Raman shift (cm-1)
D
G
D'
D
c)
5 µm
d)
G-channels etching
Pattern for ohmics
Ohmic contacts
Passivation
e)
20 µm
f)
G (µS)
gm (mS/V)
VLG (V)

Figure 1.

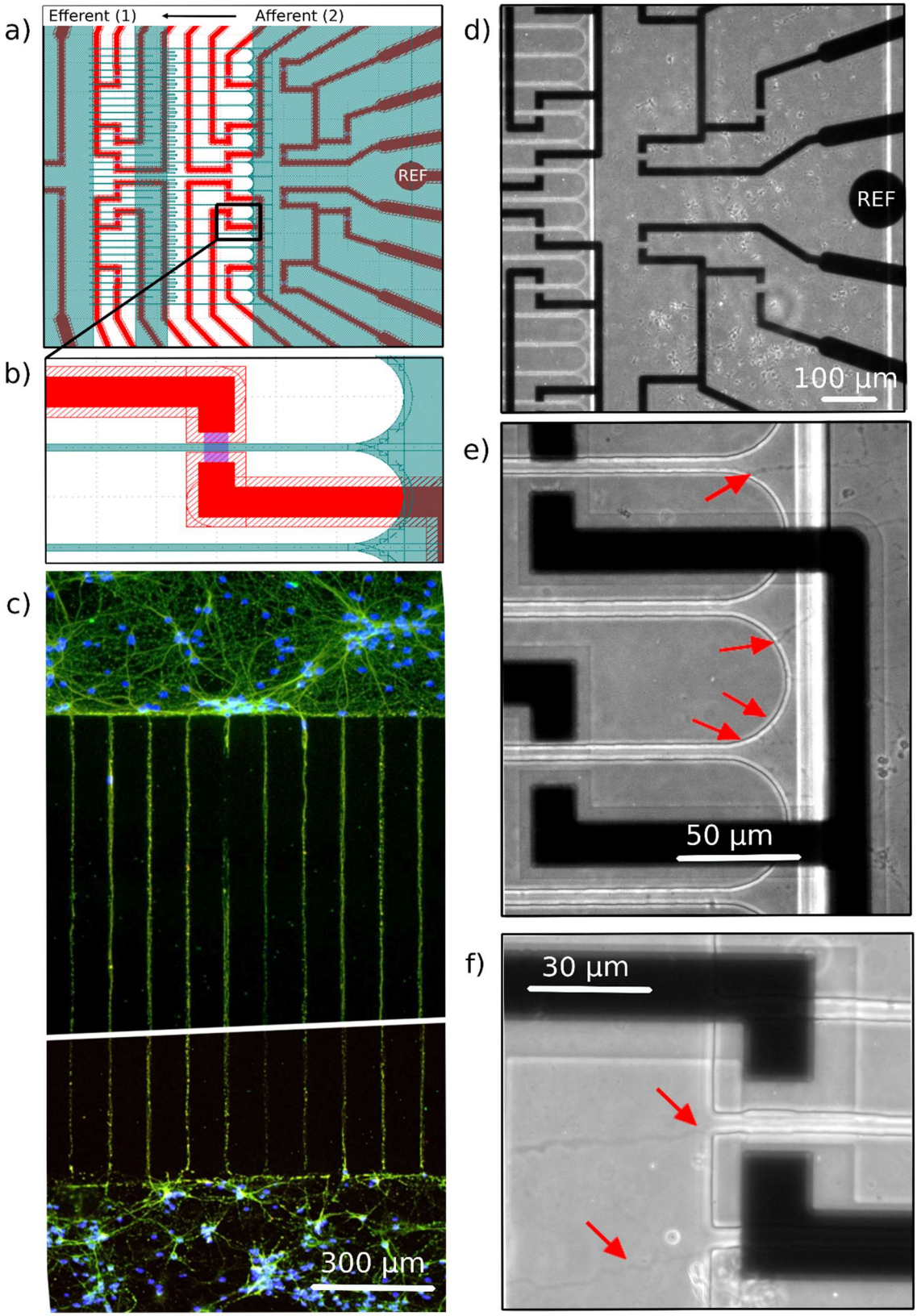

Figure 2.

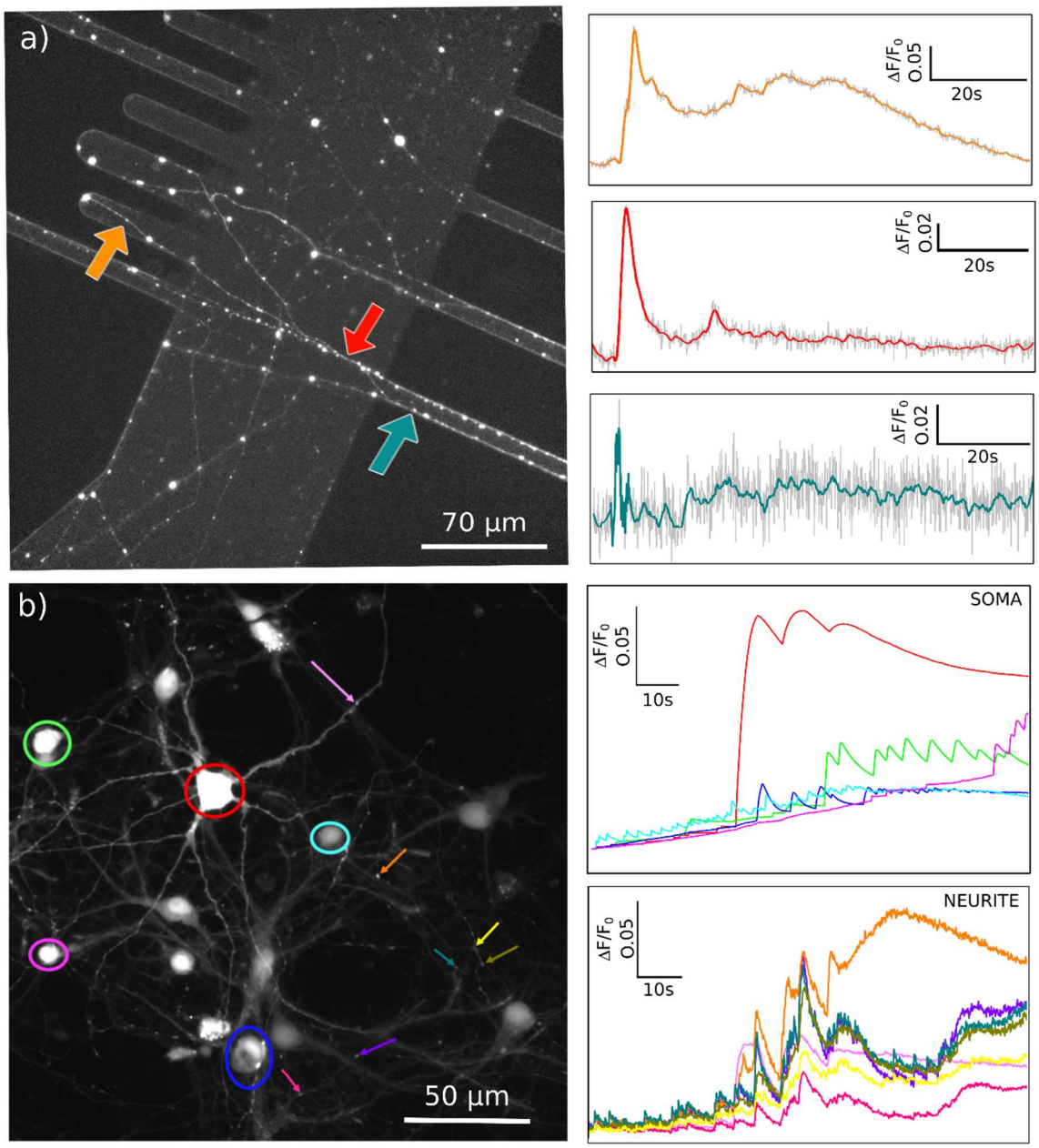
a)
70 µm
ΔF/F0
0.05
20s
ΔF/F0
0.02
20s
ΔF/F0
0.02
20s
b)
50 µm
SOMA
ΔF/F0
0.05
10s
NEURITE
ΔF/F0
0.05
10s

Figure 3.

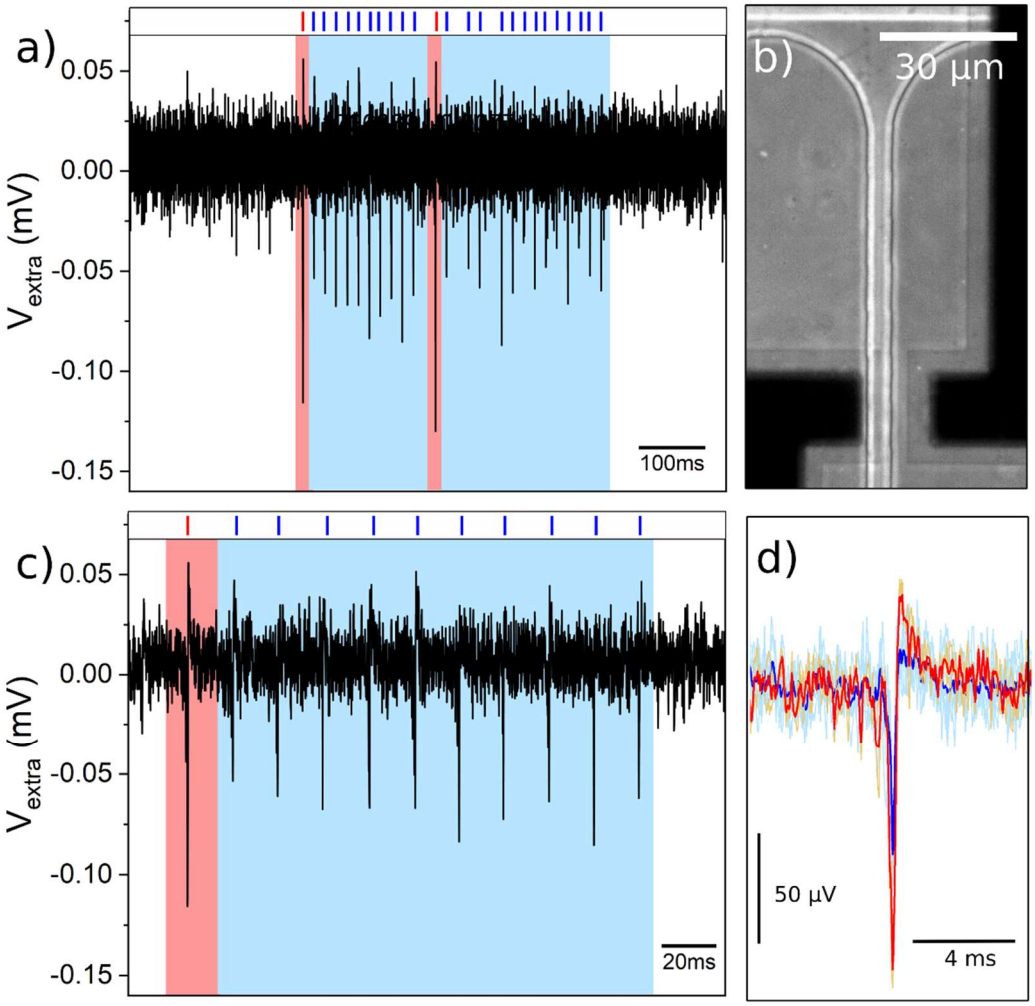
a)
0.05
0.00
-0.05
-0.10
-0.15
V_{extra} (mV)
100ms
b)
30 µm
c)
0.05
0.00
-0.05
-0.10
-0.15
V_{extra} (mV)
20ms
d)
50 µV
4 ms

Figure 4.

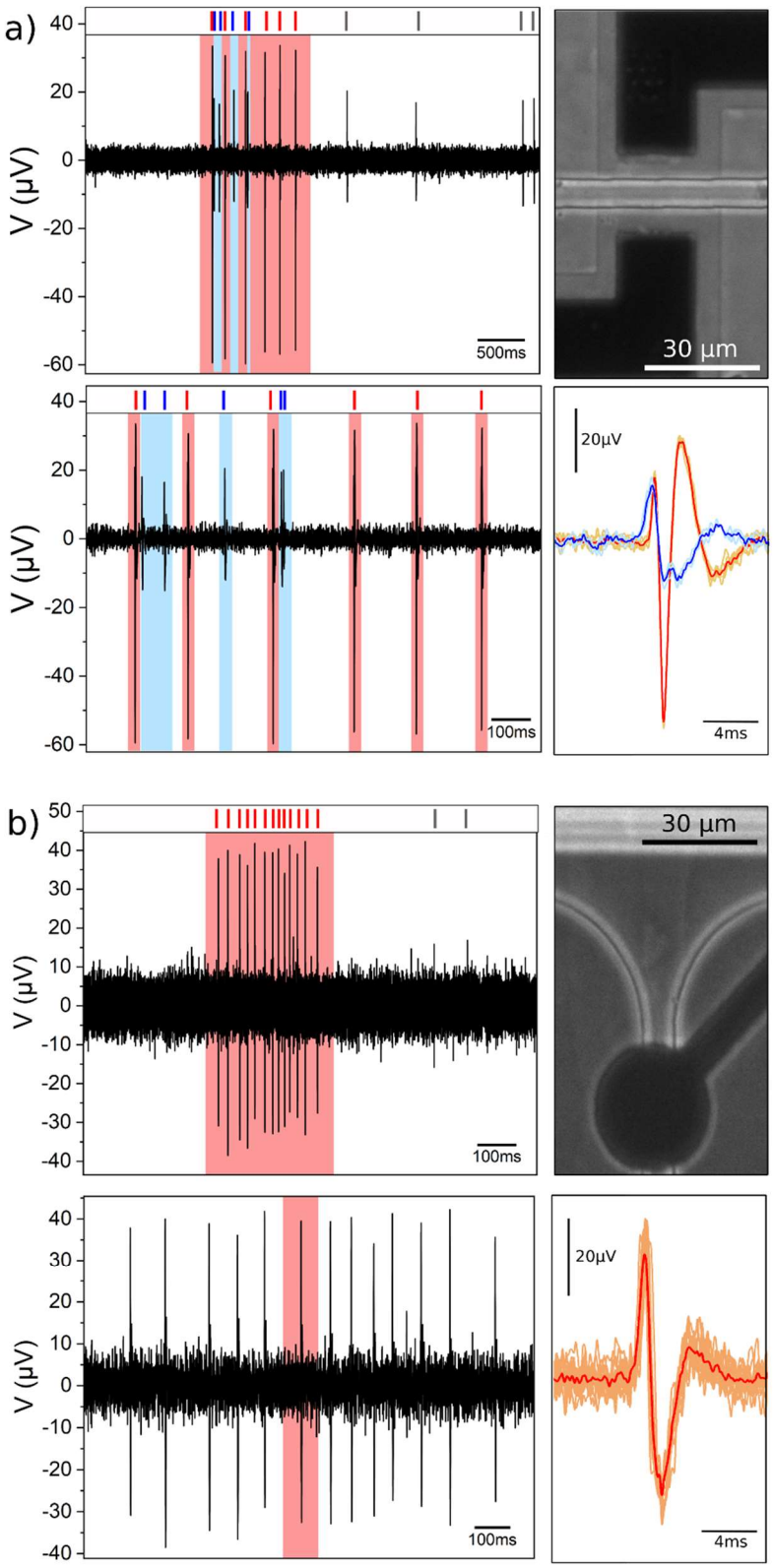

Figure 5.

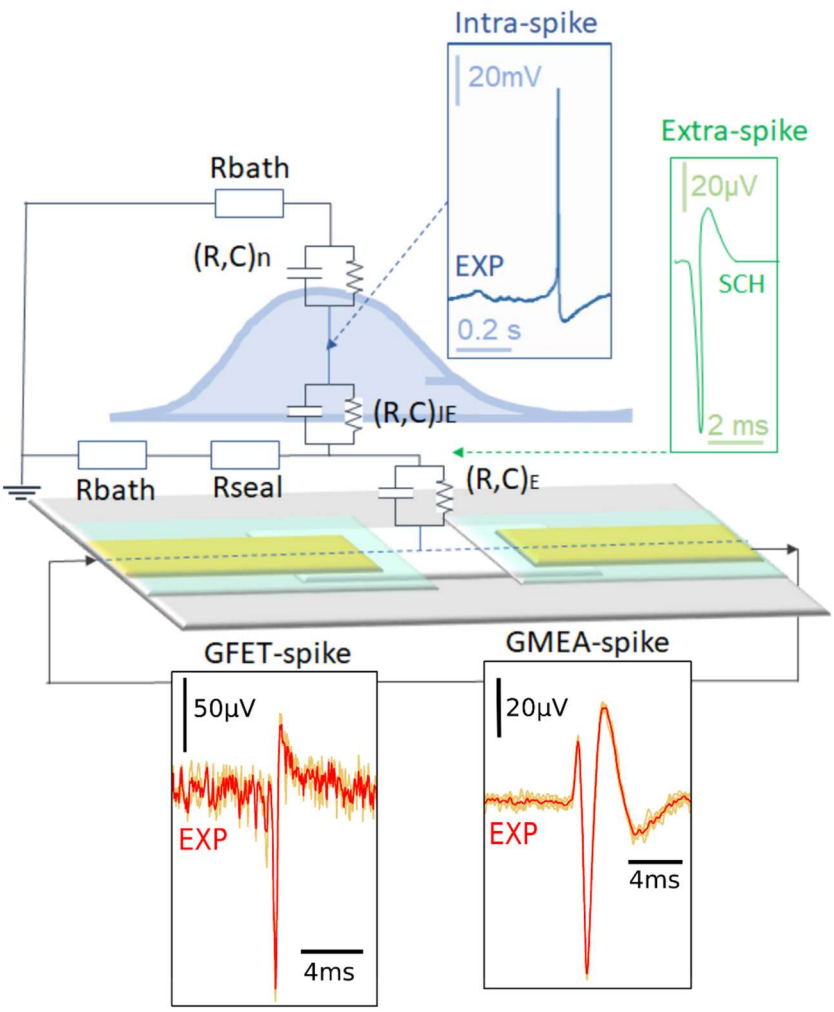

Figure 6.

6. Experimental Section

GFET chip fabrication: Sapphire chips were diced, cleaned in acetone and isopropanol in an ultrasonic bath for one minute each, then alignment marks were defined by laser lithography followed by titanium (10nm) and nickel (15nm) evaporation. After an identical cleaning step, graphene was transferred onto the chips using the PMMA carrier method. After overnight removal of the PMMA layer in acetone, residues were decomposed by annealing at 350°C for 2h in UHV. GFET channels were defined by laser lithography, removing the photoresist on top of the future transistors and protected with an evaporated 10nm gold layer. After lifting the gold, the graphene outside the channel was etched with a 1min 10W O_2 RIE plasma. Gold was then

etched from the graphene using a commercial potassium iodide solution (Transene Company Inc. Gold etch TFA, 28 angströms/s etch rate). The samples were then annealed again in the same conditions to remove photoresist residues and ensure a good electrical contact. Ohmics were fabricated by UV lithography followed by an evaporation of 0.5nm Ti, 5nm Pd and 44.5nm Au for a total thickness of 50nm and lifted-off in NMP (*N*-Methyl-2-pyrrolidone) heated to 80°C. Contact lines were passivated using SU8 - 2015 (Microchem) diluted to a 7:23.5 weight ratio with SU8 Thinner (Microchem). Exposed resist was measured to be ~ 200nm high after exposure with a mechanical profilometer. S1818 photoresist was coated onto contact pads and a layer of 2nm Hafnium oxide was deposited on the chip by ALD. Finally, the resist on the pads was removed in acetone, IPA and nitrogen dried. Between each day of manufacturing and until use after completion, the GFET chips were stored under primary vacuum.

Microfluidic chip fabrication: For our mold fabrication we used MR-DWL (Microresist technology GmbH) photoresist line in two thicknesses 5 µm and 40 µm. This product is an epoxy resist similar to SU8 but is sensitive at 405 nm and designed for laser lithography. Alignment marks were done on the back side of the wafer and two subsequent laser lithography steps first for the 5 µm layer (defining the inter-chamber microgrooves) and then for the 40 µm layer (defining the soma chambers and seeding wells) were performed. The mold was hard baked at 180°C on a hotplate for 30min according to the manufacturer guidelines. Following this PDMS was prepared with a Sylgard 108 kit (Dow Crowning) and poured onto the mold. The preparation was baked in an oven for 2h at 80°C to achieve the polymerization. The chips were then cut, peeled off and wells punched with a biopsy puncher. Residues were removed by putting and peeling repetitively Kapton tape and sonicated for 2mins in 70% ethanol for sterilization.

Culture preparation: The day before the culture, the GFET chips were put on the hot plate at 180°C to remove any adsorbed water. Following this, a drop of sterile distilled water was spread on top of the chips and covered with the microfluidics which allowed to move it and align the

channels with the transistors under an inverted microscope. The chips were left to dry completely under the biosafety cabinet. Next, the assembled devices were placed in a O_2 plasma reactor and processed with the following parameters (100% O_2, 120 mTorr, 120 s, March PX500) to ease the channels filling. The chips were brought back to the biosafety cabinet immediately, transferred to their culture dish and filled with a solution of poly-(L)-lysine (PLL, 0.1 mg/mL in DI water, Sigma-Aldrich). The dish was sealed as air-tight as possible with parafilm and left under the hood for the night. The day of the culture, the PLL was removed and the chip was rinsed 3 times with sterile DI water.

Cell culture: Hippocampal and cortical neurons were extracted from E16 mouse embryos, dissociated according to our previously reported protocol,[26] counted and diluted to 10 million cells/mL in MEM supplemented with 10% horse serum, 1% glutamine and 0.5% peniciline/streptomycine (all cell culture medium and supplements were supplied by ThermoFisher Scientific Inc.). 10µL of cell suspension was injected in one well for each somatic chamber, pipette tip away from the chamber entrance, and left alone for one minute under the biosafety hood. Then, the operation was repeated at the other end of the chamber and the chip was left untouched for 10min, allowing the cells to settle and adhere without flow. The chips were transferred in a humidified 5% CO2 incubator for 2h and were filled next with 100µL of glia-conditioned Neurobasal media in each well. Every 48h the samples were checked and media refilled depending on the apparent evaporation of liquid in each well.

Immunofluorescence: Cells were fixed with 4% paraformaldehyde solution for 15min, chip still assembled and rinsed three times with PBS. Samples could be conserved about two weeks before disassembling in PBS. To do so, the substrate was held against a flat cleanroom wiper and the PDMS corners were lightly lifted by hand. After some time, the central area of the microfluidic chip comes off while keeping a non-negligible part of the neurites in the

microchannels which can be marked efficiently. The neurons were then permeabilized in PBS-0.25% Triton X100, blocked in PBS-2% bovine serum albumin and immunostained with anti-alpha tubulin (1:1000, Millipore) and DAPI to label the cytoskeleton and the nucleus respectively. All liquid operations of the 30mm coverslips were performed upside-down on drops placed on Parafilm in order to reduce the used volume. After rinsing in PBS, coverslips were mounted on glass slides and imaged using an Andor Zyla scientific camera, controlled by Andor Solis and an Olympus BX51 microscope. The images were processed with ImageJ.

Data Acquisition: Samples were taken out of the incubator and covered with a teflon membrane (fluorinated ethylene-propylene membrane, Honeywell International Inc.) under a biosafety cabinet to preserve sterility of the culture media. Then, samples were placed in a Faraday cage equipped with micromanipulated probes and one transistor known to be connected and below a microchannel was contacted. Data was acquired with a NI-PCIe-7852 configured with custom LABVIEW VIs for parameter sweep measurements (transfer curves) and for time recordings (spike measurements). In transistor mode, current was amplified with a variable gain current amplifier (Femto Messtechnik GmbH, DLPCA-200) to match the -10 V/+10 V input range of the DAQ card. Transfer curves were obtained by sweeping V_{GS} at 200 Hz with a 0.001 V step across the measured range. The tuning point was chosen with the transfer curve, the polarization and amplifier gain were set so that the baseline of the DC current at the maximum transconductance was about 9 µA (which maximized the SNR ratio without saturating the amplifier). In electrode mode, signals were amplified with a x100 gain low noise pre-amplifier (NF Electronic Instruments, LI-75A) and send to the same DAQ system.

All electrical and optical recordings were conducted under static fluid. Additionally, all acquisitions started 5 mins after placing the chip under the electrical or optical setup to ensure the cells recover a static fluidic environment.

References

1. Park, S. *et al.* One-step optogenetics with multifunctional flexible polymer fibers. *Nat Neurosci* **20**, 612–619 (2017).
2. Boi, F. *et al.* Multi-shanks SiNAPS Active Pixel Sensor CMOS probe: 1024 simultaneously recording channels for high-density intracortical brain mapping. *bioRxiv* 749911 (2019) doi:10.1101/749911.
3. Jun, J. J. *et al.* Fully integrated silicon probes for high-density recording of neural activity. *Nature* **551**, 232–236 (2017).
4. Obien, M. E. J., Deligkaris, K., Bullmann, T., Bakkum, D. J. & Frey, U. Revealing neuronal function through microelectrode array recordings. *Frontiers in Neuroscience* **8**, (2015).
5. Bakkum, D. J. *et al.* Tracking axonal action potential propagation on a high-density microelectrode array across hundreds of sites. *Nat Commun* **4**, 2181 (2013).
6. Steinmetz, N. A. *et al.* Neuropixels 2.0: A miniaturized high-density probe for stable, long-term brain recordings. *Science* **372**, eabf4588 (2021).
7. van Daal, R. J. J. *et al.* Implantation of Neuropixels probes for chronic recording of neuronal activity in freely behaving mice and rats. *Nat Protoc* **16**, 3322–3347 (2021).
8. Charvet, G. *et al.* BioMEA^{TM}: A versatile high-density 3D microelectrode array system using integrated electronics. *Biosensors and Bioelectronics* **25**, 1889–1896 (2010).
9. Spira, M. E. & Hai, A. Multi-electrode array technologies for neuroscience and cardiology. *Nature Nanotech* **8**, 83–94 (2013).
10. Jorfi, M., Skousen, J. L., Weder, C. & Capadona, J. R. Progress Towards Biocompatible Intracortical Microelectrodes for Neural Interfacing Applications. *J Neural Eng* **12**, 011001 (2015).

11. Patolsky, F. *et al.* Detection, Stimulation, and Inhibition of Neuronal Signals with High-Density Nanowire Transistor Arrays. *Science* **313**, 1100–1104 (2006).
12. Fromherz, P., Offenhausser, A., Vetter, T. & Weis, J. A neuron-silicon junction: a Retzius cell of the leech on an insulated-gate field-effect transistor. *Science* **252**, 1290–1293 (1991).
13. Delacour, C. *et al.* Neuron-Gated Silicon Nanowire Field Effect Transistors to Follow Single Spike Propagation within Neuronal Network. *Advanced Engineering Materials* **23**, 2001226 (2021).
14. Benfenati, V. *et al.* A transparent organic transistor structure for bidirectional stimulation and recording of primary neurons. *Nature Mater* **12**, 672–680 (2013).
15. Cohen-Karni, T., Qing, Q., Li, Q., Fang, Y. & Lieber, C. M. Graphene and Nanowire Transistors for Cellular Interfaces and Electrical Recording. *Nano Lett.* **10**, 1098–1102 (2010).
16. Veliev, F. *et al.* Recording Spikes Activity in Cultured Hippocampal Neurons Using Flexible or Transparent Graphene Transistors. *Front. Neurosci.* **11**, (2017).
17. Hébert, C. *et al.* Flexible Graphene Solution-Gated Field-Effect Transistors: Efficient Transducers for Micro-Electrocorticography. *Advanced Functional Materials* **28**, 1703976 (2018).
18. Masvidal-Codina, E. *et al.* High-resolution mapping of infraslow cortical brain activity enabled by graphene microtransistors. *Nature Mater* **18**, 280–288 (2019).
19. Lu, Y., Lyu, H., Richardson, A. G., Lucas, T. H. & Kuzum, D. Flexible Neural Electrode Array Based-on Porous Graphene for Cortical Microstimulation and Sensing. *Sci Rep* **6**, 1–9 (2016).
20. Kireev, D. *et al.* Graphene transistors for interfacing with cells: towards a deeper understanding of liquid gating and sensitivity. *Sci Rep* **7**, 1–12 (2017).

21. Wang, R. *et al.* Ultrasensitive Graphene Optoelectronic Probes for Recording Electrical Activities of Individual Synapses. *Nano Lett.* **18**, 5702–5708 (2018).

22. Veliev, F. *et al.* Sensing ion channel in neuron networks with graphene field effect transistors. *2D Mater.* **5**, 045020 (2018).

23. Pampaloni, N. P. *et al.* Single-layer graphene modulates neuronal communication and augments membrane ion currents. *Nature Nanotech* **13**, 755–764 (2018).

24. Kuzum, D. *et al.* Transparent and flexible low noise graphene electrodes for simultaneous electrophysiology and neuroimaging. *Nat Commun* **5**, 1–10 (2014).

25. Thunemann, M. *et al.* Deep 2-photon imaging and artifact-free optogenetics through transparent graphene microelectrode arrays. *Nat Commun* **9**, 2035 (2018).

26. Veliev, F., Briançon-Marjollet, A., Bouchiat, V. & Delacour, C. Impact of crystalline quality on neuronal affinity of pristine graphene. *Biomaterials* **86**, 33–41 (2016).

27. Fabbro, A. *et al.* Graphene-Based Interfaces Do Not Alter Target Nerve Cells. *ACS Nano* **10**, 615–623 (2016).

28. Bourrier, A. *et al.* Monolayer Graphene Coating of Intracortical Probes for Long-Lasting Neural Activity Monitoring. *Advanced Healthcare Materials* **8**, 1801331 (2019).

29. Taylor, A. M. *et al.* A microfluidic culture platform for CNS axonal injury, regeneration and transport. *Nat Methods* **2**, 599–605 (2005).

30. Kamande, J. W., Nagendran, T., Harris, J. & Taylor, A. M. Multi-compartment Microfluidic Device Geometry and Covalently Bound Poly-D-Lysine Influence Neuronal Maturation. *Frontiers in Bioengineering and Biotechnology* **7**, (2019).

31. Peyrin, J.-M. *et al.* Axon diodes for the reconstruction of oriented neuronal networks in microfluidic chambers. *Lab Chip* **11**, 3663–3673 (2011).

32. Virlogeux, A. *et al.* B41 HD on chip : reconstituting the cortico-striatal network on microfluidics to study intracellular trafficking and synaptic transmission. *J Neurol Neurosurg Psychiatry* **87**, A23–A24 (2016).

33. Holloway, P. M. *et al.* Advances in microfluidic in vitro systems for neurological disease modeling. *Journal of Neuroscience Research* **99**, 1276–1307 (2021).

34. Virlogeux, A. *et al.* Reconstituting Corticostriatal Network on-a-Chip Reveals the Contribution of the Presynaptic Compartment to Huntington's Disease. *Cell Reports* **22**, 110–122 (2018).

35. Moutaux, E., Charlot, B., Genoux, A., Saudou, F. & Cazorla, M. An integrated microfluidic/microelectrode array for the study of activity-dependent intracellular dynamics in neuronal networks. *Lab Chip* **18**, 3425–3435 (2018).

36. Pan, L., Alagapan, S., Franca, E., Brewer, G. J. & Wheeler, B. C. Propagation of action potential activity in a predefined microtunnel neural network. *J. Neural Eng.* **8**, 046031 (2011).

37. Kanagasabapathi, T. T., Ciliberti, D., Martinoia, S., Wadman, W. J. & Decré, M. M. J. Dual-Compartment Neurofluidic System for Electrophysiological Measurements in Physically Segregated and Functionally Connected Neuronal Cell Culture. *Frontiers in Neuroengineering* **4**, 13 (2011).

38. Suk, J. W. *et al.* Transfer of CVD-Grown Monolayer Graphene onto Arbitrary Substrates. *ACS Nano* **5**, 6916–6924 (2011).

39. Ferrari, A. C. *et al.* Raman Spectrum of Graphene and Graphene Layers. *Phys. Rev. Lett.* **97**, 187401 (2006).

40. Calizo, I., Bao, W., Miao, F., Lau, C. N. & Balandin, A. A. The effect of substrates on the Raman spectrum of graphene: Graphene- on-sapphire and graphene-on-glass. *Appl. Phys. Lett.* **91**, 201904 (2007).

41. Bourrier, A. *et al.* Introducing a biomimetic coating for graphene neuroelectronics: toward in-vivo applications. *Biomed. Phys. Eng. Express* (2019) doi:10.1088/2057-1976/ab42d6.

42. Heim, M. *et al.* Combined macro-/mesoporous microelectrode arrays for low-noise extracellular recording of neural networks. *Journal of Neurophysiology* **108**, 1793–1803 (2012).

43. Du, X. *et al.* Graphene microelectrode arrays for neural activity detection. *J Biol Phys* **41**, 339–347 (2015).

44. Schaefer, N. *et al.* Multiplexed neural sensor array of graphene solution-gated field-effect transistors. *2D Mater.* **7**, 025046 (2020).

45. Garcia-Cortadella, R. *et al.* Switchless Multiplexing of Graphene Active Sensor Arrays for Brain Mapping. *Nano Lett.* **20**, 3528–3537 (2020).

Supporting Information

A multifunctional hybrid graphene and microfluidic platform to interface topological neuron networks

Supplementary figures from S1 to S9

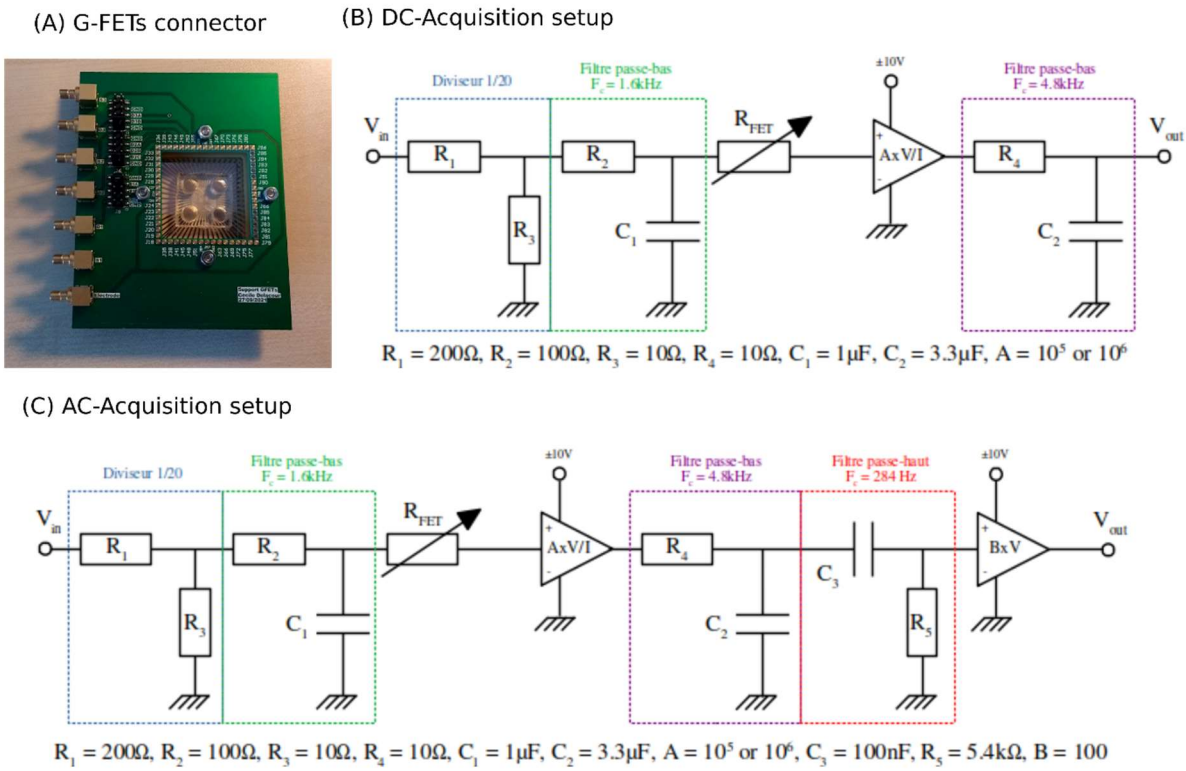

Figure S1. Schematics of the acquisition setups used for single-units detection with the GFETs. A) Optical picture shows the hybrid GFET and µfluidic circuit in place within the dedicated home-made connector. The chip is 44×44 mm² large and contained 64 ohmics for the transistors. B-C) The equivalent electrical circuits used to monitor the conductance of the neuron-gated GFETs. An additional filtering stage could be used after the current-voltage converter to remove the DC component and further amplify the signals of interest in the kHz range(C).

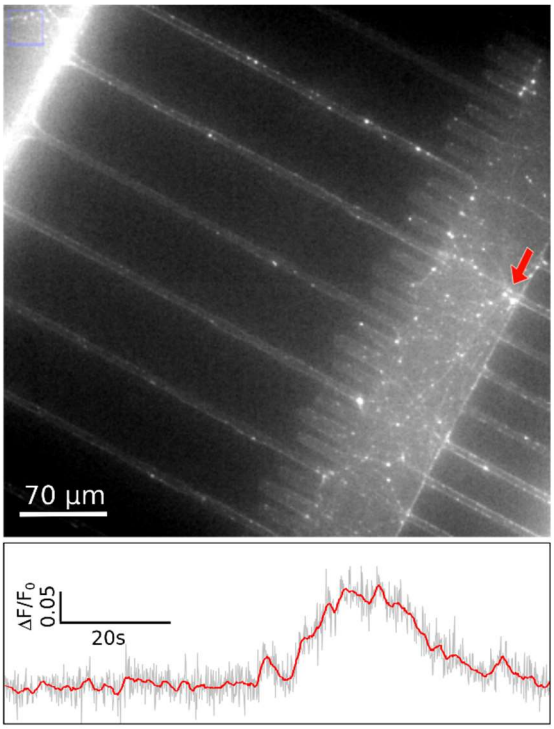

Figure S2. Intracellular Ca^{2+} imaging (frontside) within topological networks. The neurons have been loaded with Fluo4-AM and recorded in HBSS-HEPES at room temperature and at DIV14 (details in the experimental section). The top FITC-image zooms in the synaptic chamber, showing the Fluo4-loaded neurites spreading through the expected afferent and efferent fluidic microchannels that finally meet in the synaptic chamber (20× magnification). Bottom is an example of temporal evolution of the fluorescence intensity ratio ΔF/F0 measured along a single neurite in the synaptic chamber (as indicated with the arrow). The time-trace shows the variation of fluorescent intensity related to Ca2+ transient currents, that could be expected in front-side imaging configuration (illumination through the PDMS circuit).

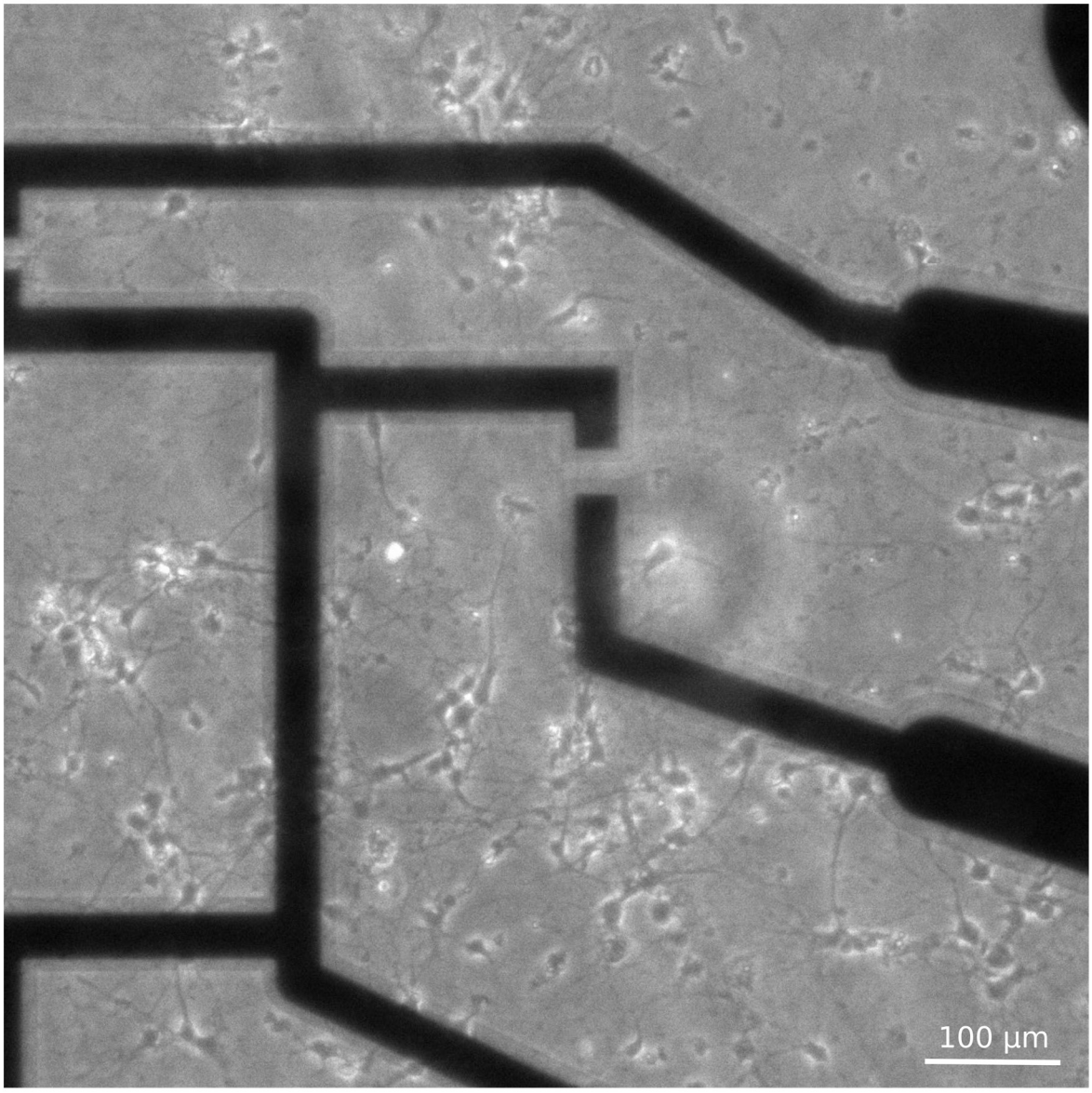

Figure S3. Zoomed-view on neurons, cultured within the microfluidic circuit assembled with the GFET substrate. Extracted from figure 2.

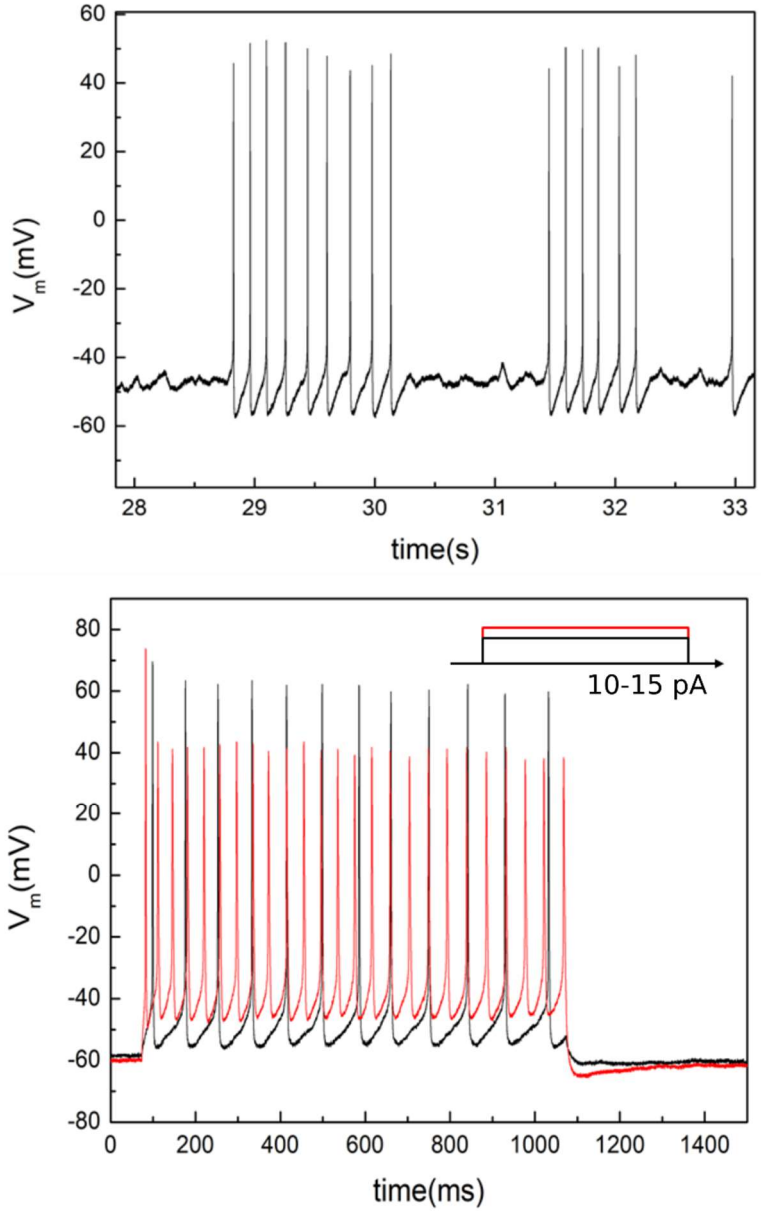

Figure S4. Patch-Clamp measurement of intracellular voltage within neurons cultured 12 days in a petri dish. Acquisition is obtained in whole cell configuration, and both voltage (top) and current (bottom) clamp have been used. On the top graph, the membrane potential is varied from -57 mV to slightly higher values until it trigs the emission of spike train. Interval between each APs is highly regular (143 ms), while amplitude varies of about 10%. The bottom graph, shows the intracellular voltage response when applying a current ramp of 10 pA (black line) and 15pA (red line). When no current is applied the resting voltage remains fixed is at -57mV. The 1s-duration current step trigs a series of action potentials. The first peak exhibits the highest amplitude (ΔV_{intra}= 130 mV). The amplitude of the successive spikes ranges around 120mV and 100mV ±5mV for each value of the current plateau (10 and 15pA respectively).

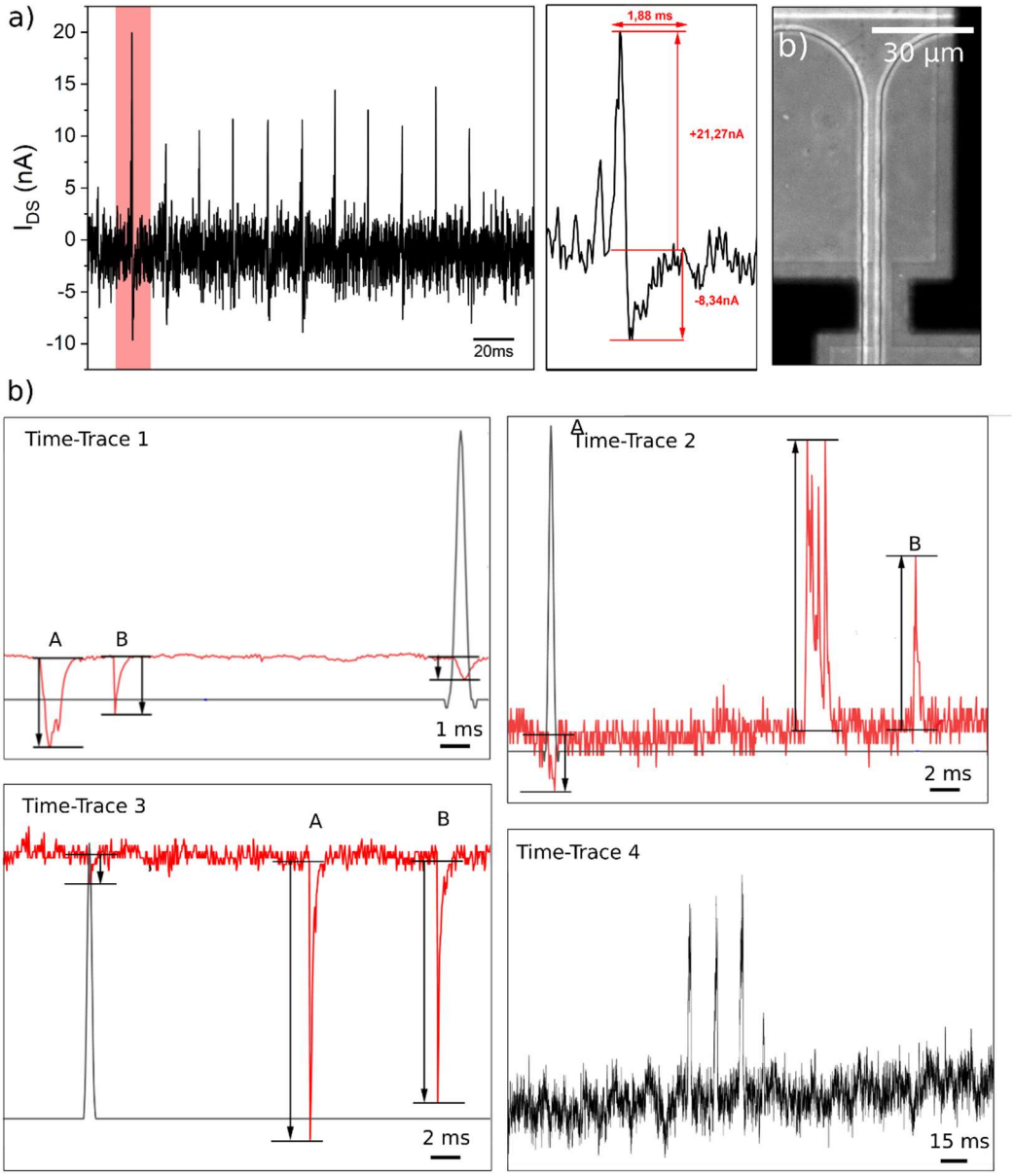

Figure S5. Single-unit recordings with the GFETs. Current-time traces of neuron-gated GFETs showing several spike forms of detected neuronal signals: raw data in panel (a) and (b) are exploited within figure 4 and table 1 respectively For the recordings of panel (b), voltage impulses (1 mV and 1ms) are applied with the liquid gate (black line on time-trace 1, 2 and 3) to assess the amplitude and polarity of the GFET response also reported within table 1. From time-trace 1 to 4, the recording configuration is as the following: (1 and 2) V_{DS}= 60mV, V_{LG}=660mV, f=15kHz, DIV7; (3) V_{DS}= 75mV, V_{LG}=500mV; (4) V_{DS}= 75mV, V_{LG}=750mV, f=50kHz, DIV10.

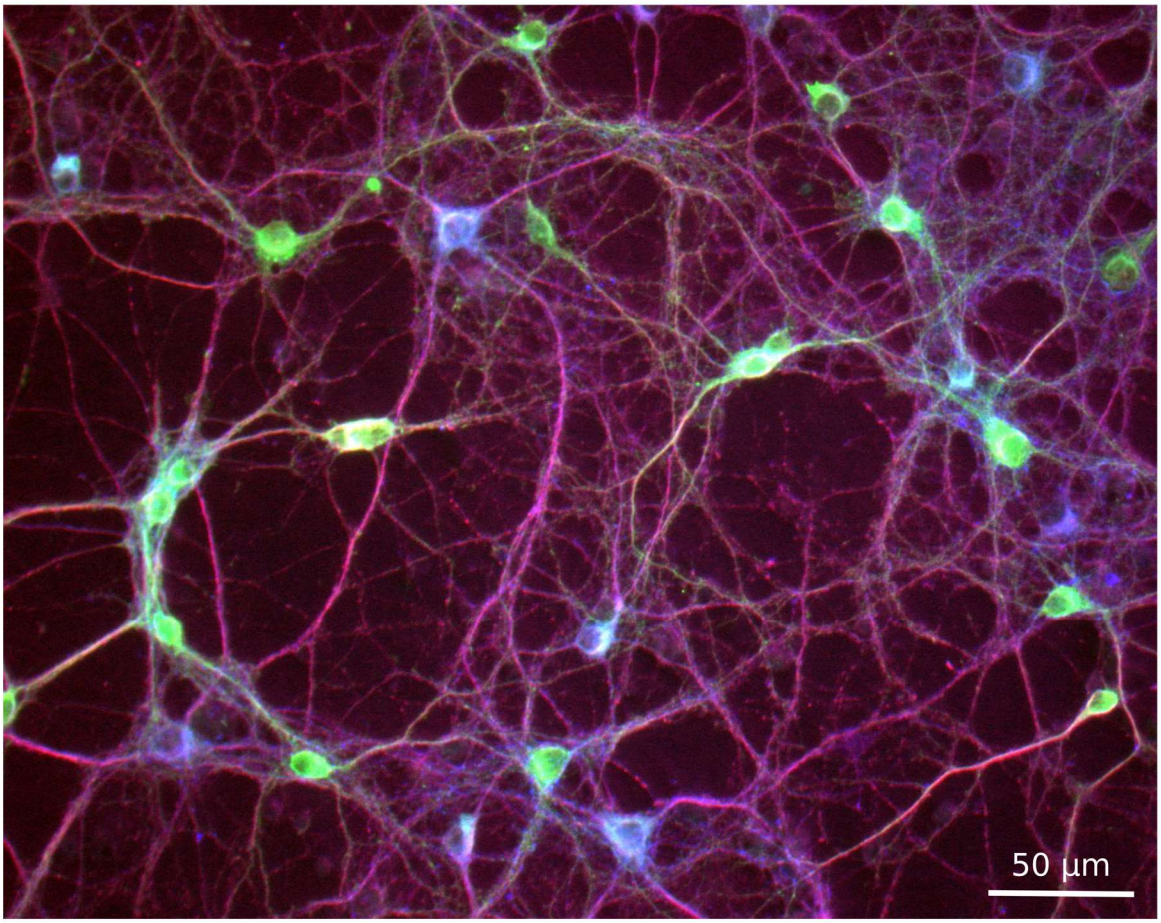

Figure S6. Post hoc immunofluorescence of primary hippocampal neurons, cultured 19 days on poly-L-lysin coated glass coverslip. Cells were stained with anti-alpha tubulin (1:1000, Millipore) , anti-CamKII and anti-GAD (1:300) to label the neurites and to identify the excitator and inhibitor neurons.

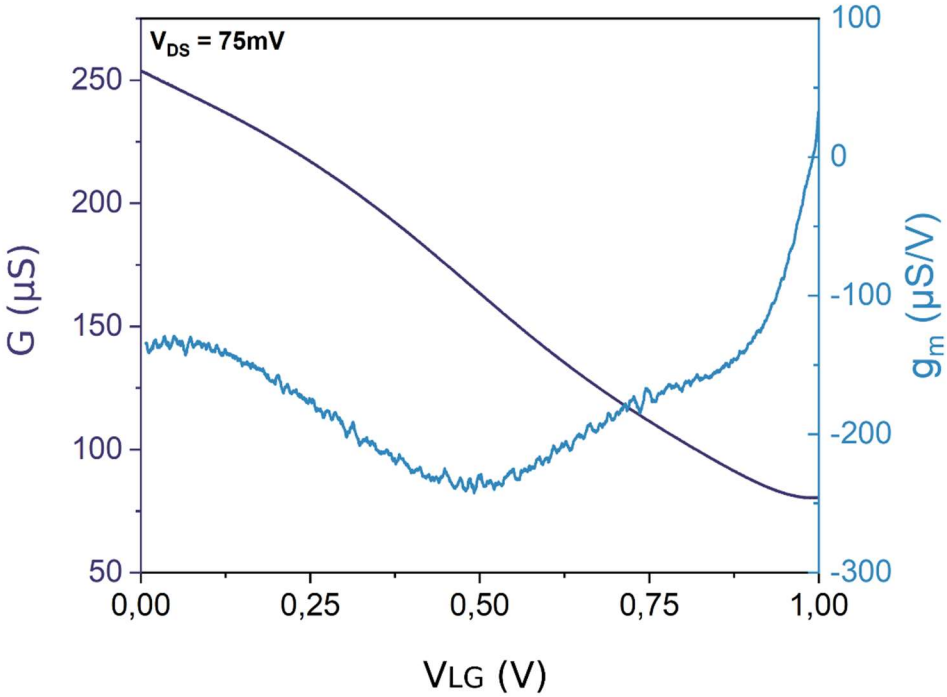

Figure S7. In-situ measurements of the GFET conductance and normalized transconductance as a function of the liquid gate voltage. The GFETs array is combined with the microfluidic circuit and neurons are maintained in the culture medium for 10 days. The 100 µm wide Au-electrode located in the somatic chamber (figure 2) is used as a reference and liquid gate electrode.

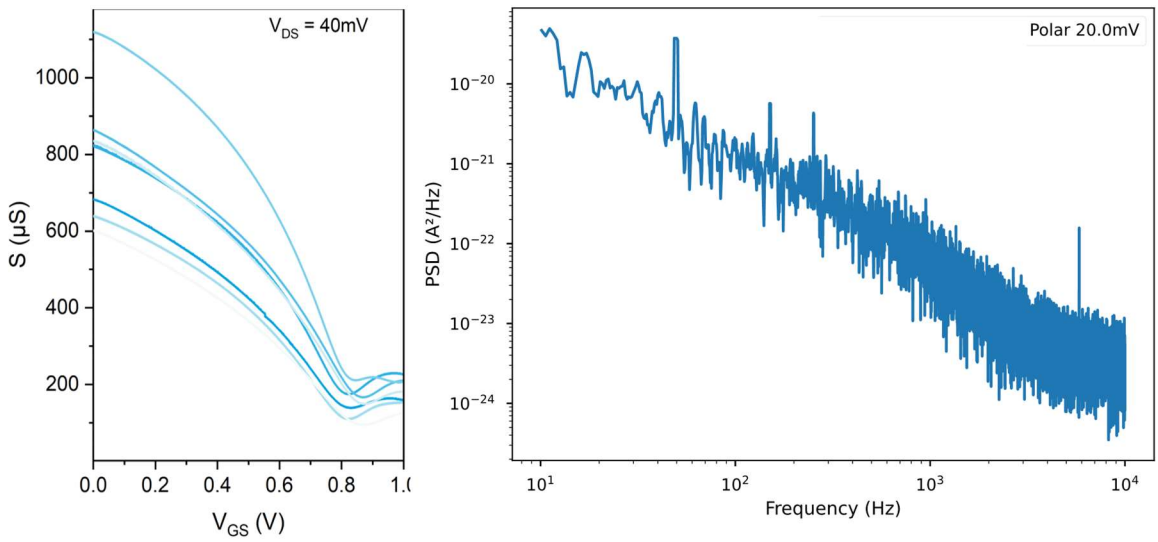

Figure S8. Additional electrical characterizations of graphene FETs. (left) Conductance as function of the liquid gate voltage for several devices of a same array and (right) power spectral density of the drain current. GFET is polarized at 40 mV and 100 mV respectively. An Ag/AgCl electrode is used as the reference electrode.

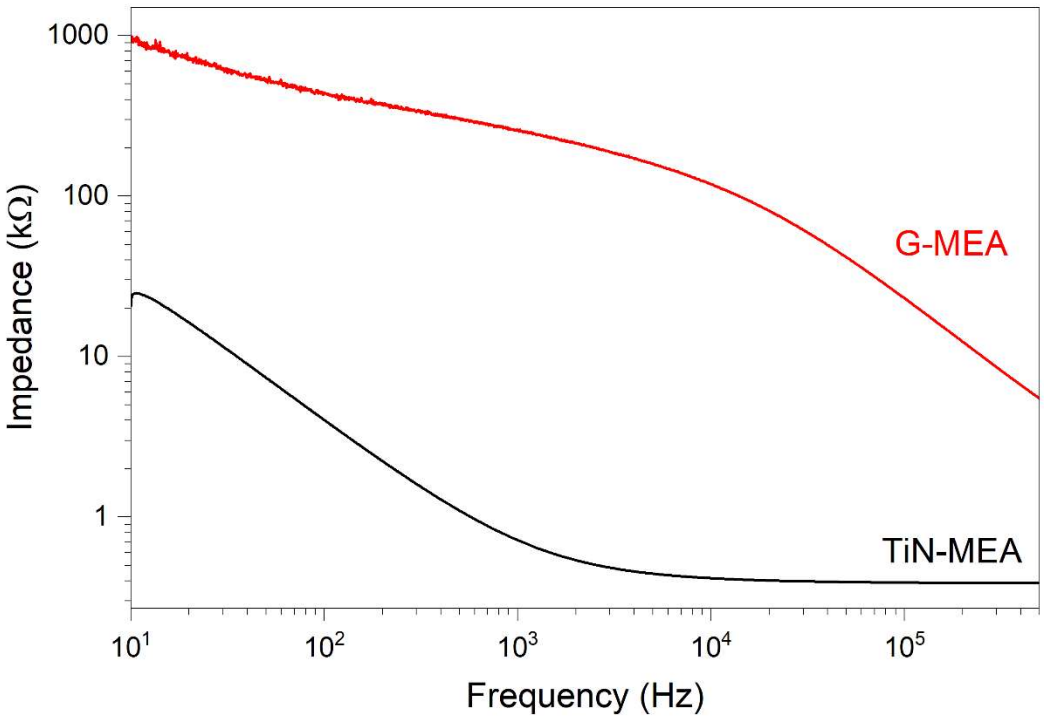

Figure S9. Electrochemical impedance spectroscopy. Bode plots of the electrochemical impedance of the graphene (S=200 µm²) and TiN (S=706 µm²) against a 4 mm² Pt quasi-reference electrode, measured in PBS, at 50 and 35 mV respectively. The impedance is higher for the graphene devices over the entire spectral range, as expected from the previously published results.[43]